Electrochemically Prepared Pore Arrays for Photonic-Crystal Applications

R.B. Wehrspohn and J. Schilling

Introduction

In the last few years, photonic crystals have gained considerable interest due to their ability to "mold the flow of light."[1] Photonic crystals are physically based on Bragg reflections of electromagnetic waves. In simple terms, a one-dimensional (1D) photonic crystal is a periodic stack of thin dielectric films with two different refractive indices, n_1 and n_2. The two important geometrical parameters determining the wavelength of the photonic bandgap are the lattice constant, $a = d_1(n_1) + d_2(n_2)$, and the ratio of d_1 to a (where d_1 is the thickness of the layer with refractive index n_1, and d_2 is the thickness of layer n_2). For a simple quarter-wavelength stack, the center wavelength λ of the 1D photonic crystal would be simply $\lambda = 2n_1d_1 + 2n_2d_2$. In the case of 2D photonic crystals, the concept is extended to either airholes in a dielectric medium or dielectric rods in air. Therefore, ordered porous dielectric materials like porous silicon or porous alumina are *intrinsically* 2D photonic crystals.

Electrochemically grown pores in metals and semiconductors[2,3] have been studied for about 50 years. However, only in the last 10 years have intense research efforts enabled the preparation of *ordered* arrays of pores with pore diameters in the range of a few nanometers to some tens of micrometers. The most studied materials are porous alumina and macroporous silicon.

Porous alumina has been known for more than a century, but only in 1995 was it first observed that ordered arrays of porous alumina could be achieved.[4] This ordering was initially by self-organization, and the ordered domains were in the micrometer range. However, electron-beam lithography[5] and a related new technique, nanoindentation,[6] allowed the preparation of monodomain porous alumina structures with sizes in the micrometer range.

Macroporous silicon was pioneered in the early 1990s by Lehmann and Föll.[7] Very regular pore arrays in the micrometer range have been obtained by photolithographic prepatterning. These pores were called macropores (in contrast to microporous silicon, which is a sponge-like nanostructured material with photoluminescent properties that was also intensively studied in the early 1990s).[8]

Moreover, recently a few other semiconductors like InP, GaAs, and GaP have been shown to exhibit micrometer-sized pores.[9,10] Whereas standard nanostructuring techniques are limited to small pore aspect ratios ($h/d < 40$), and resolutions are limited by lithographic tools, electrochemically prepared pores exhibit high aspect ratios of 100–10,000 and inherent short-range order. In the following, two materials will be discussed in detail: macroporous silicon and porous alumina. Due to the regular pore arrangements, these materials are extremely well suited as photonic crystals.

Macroporous Silicon

Porous silicon formed by the anodization of *p*-type silicon in hydrofluoric acid has been studied by numerous groups. A current state-of-the-art summary is given by Allongue.[11] Three different pore-formation regimes have been observed experimentally as a function of the dopant concentration. For degenerately doped *p*-type silicon, a special type of mesopore observed experimentally has been attributed to tunneling of holes through the space-charge region.[12] For moderately doped *p*-type silicon, nanopore formation is observed with pores in the range of 2–100 nm. For highly resistive crystalline and amorphous *p*-type silicon, macropore formation (0.4–10 μm in diameter) is observed below a thin layer of nanopores.[13,14] Previously, macropore formation in low-doped Si had been reported in anhydrous electrolyte.[15,16] The wall thickness is about two times the space-charge region, whereas the interpore distance is governed by the properties of the silicon–electrolyte interface, the resistivities of the silicon wafer, and the properties of the electrolyte.[17,18] A detailed description of macroporous silicon formation in *n*-type Si can be found in References 7 and 19. Since in *n*-type silicon holes are minority carriers, the holes have to be generated by back-side illumination. Then they diffuse to the etch front through the wafer. This technique puts high demands on the minority carrier diffusion length, so normally float-zone (FZ) wafers are used. Since in this technique the holes move by diffusion and not by drift as in the *p*-type case, the strong boundary condition is relaxed and thicker walls can be obtained—up to 10 times the space-charge region width.[20] To obtain ordered arrangements of pores, an *n*-type silicon wafer with ⟨100⟩ orientation is first prepatterned by standard photolithography. Subsequent alkaline etching produces inverted pyramids acting as initial pores. Under anodic bias and back-side illumination, the wafer is then etched in hydrofluoric acid. The electronic holes generated by the illumination near the back surface diffuse through the whole wafer and promote the dissolution of silicon mainly at the pore tips. As a result, pores grow straight along the [100] direction with very high aspect ratios. The arrangement of these pores can be controlled by the lithographic mask, and the pore diameter can be controlled by the illumination intensity. By controlling these parameters, variations of the pore diameter with depth can be made negligible. Figure 1 shows a scanning electron microscope (SEM) image of a porous Si sample, which was etched on 0.5 Ω cm *n*-type FZ silicon substrates having a photolithographically defined hexagonal pore arrangement. The pores have a center-to-center distance of 1.5 μm and a depth of 100 μm. The pore diameter after electrochemical etching is 0.9 μm. By subsequent oxidation/etching steps, the pore diameter is increased to up to 1.36 μm. The beveled edge in Figure 1 shows the very good depth homogeneity of the pore diameter.

Porous Alumina

Aluminum is electrochemically oxidized to alumina (Al_2O_3) under positive polari-

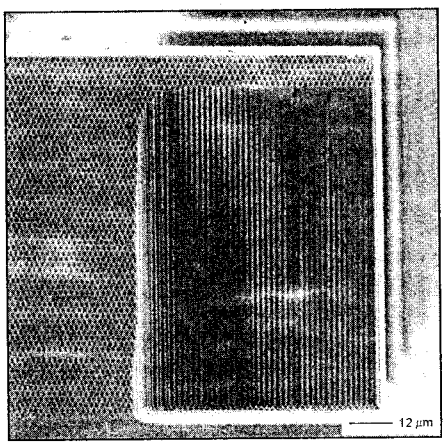

Figure 1. Scanning electron microscope (SEM) image of a perpendicular cut (right side) and beveled cut (left side) in a triangular macroporous silicon array obtained by plasma etching and subsequent polishing. Lattice constant is 1.5 μm. The pore diameter is constant throughout the entire 100-μm pore length.

zation. For certain electrolytes, which weakly dissolve the alumina, the growth of disordered pore arrangements has been observed and studied for a century now. A unique relationship between anodization voltage U and interpore distance a was found: $a = d + 2\alpha U$, where d is the diameter of the pores and $\alpha \sim 1.2$ V/nm.[3,21] In 1995, Masuda and Fukuda[4] first discovered that after long anodization times, self-ordered porous alumina films arranged in a hexagonal pattern can be obtained at the growth front. They have obtained ordered pore arrays with lattice constants of 60 nm,[22] 100 nm,[4] and 500 nm,[6] depending on the anodization conditions. The size of the pore domains increases with time and can reach micrometer size.[23] Domains touching each other have typically different orientations.[24] Mechanical stress between neighboring pores due to the volume expansion of alumina with respect to the aluminum substrate has been proposed as a mechanism for the self-ordering. For example, it is observed that the volume expansion for optimal pore growth is in the range of 1.2–1.4, that is, there is an incorporation yield of 60–70% aluminum in the alumina film.[5]

To obtain monodomain pore arrays, three strategies are possible. First, if one starts with a single-crystal seed, that is, a single pore, one would expect the other pores to arrange themselves hexagonally around it due to repulsive forces. The second strategy is based on the observation of Li et al.[23] As the anodization time increases, one should end up with a single domain since this state represents the total energy minimum of the system. Note that this assumes a monocrystalline aluminum substrate. However, both approaches seem to be quite impractical. Therefore, a third strategy is used. Knowing the optimum potential U for a certain interpore distance a, the aluminum substrate can be lithographically prepatterned. Since the feature sizes are in the range of 50 nm, electron-beam lithography prepatterning is applied.[5] Figure 2 shows a SEM image of a hexagonally ordered pore array in alumina prepared from an electron-beam lithography prepatterned substrate. The pattern has 200-nm interpore spacing, and the anodic voltage was adjusted to 85 V, based on the relationship between the interpore distance a and the potential U. The inset in Figure 2 shows the Fourier transform of the image. Very recently, Masuda et al. have shown that in addition to the hexagonal lattice, the square and honeycomb lattices can also be obtained by appropriate prepatterning, resulting in square or triangular pore shapes.[25]

Application to Photonic Crystals

In the following, we will briefly discuss the optical properties of macroporous silicon and porous alumina photonic crystals.

Macroporous Silicon

The processed macroporous Si samples shown in Figure 1 are very well suited to investigate the optical properties of light traveling perpendicular to the pores. Transmission measurements on such samples for samples with a fixed lattice constant $a = 1.5$ μm but varying pore diameters were made for different polarizations and directions. From these data, the bandgap edges were determined as a function of r/a (radius/lattice constant) for a range of wavelengths; they are indicated in Figure 3. For comparison, the theoretical predictions obtained by solving Maxwell's equations by a plane-wave expansion method are shown as solid lines.[27] There is very good agreement between theory and experiment. The 2D silicon photonic crystal exhibits a complete photonic bandgap for both polarizations, transverse magnetic (TM) and transverse electric (TE), and all in-plane directions. A maximum gap-width to midgap frequency ratio of 7% is obtained for r/a of 0.48. To obtain bandgaps in the optoelectronically interesting region around 1.3–1.55 μm, it is necessary to scale down the previously described triangular pore lattice. Recently, we have shown for the first time that it is possible to fabricate pores with a pitch of $a = 0.5$ μm.[28] The pores fabricated had a radius $r = 0.215$ μm, resulting in an r/a ratio of 0.43 and a pore depth of 100 μm.

Figure 4 shows a summary of data obtained by various authors on the bandgap-center wavelength for porous silicon and porous alumina, as a function of lattice constant a. For macroporous silicon, the obtained interpore spacings range from 500 nm to 8 μm,[29–32] leading to photonic bandgaps in the region from 1 μm to 20 μm. The electronic bandgap of silicon is at 1.1 μm, so for bandgaps below this wavelength, absorption occurs.

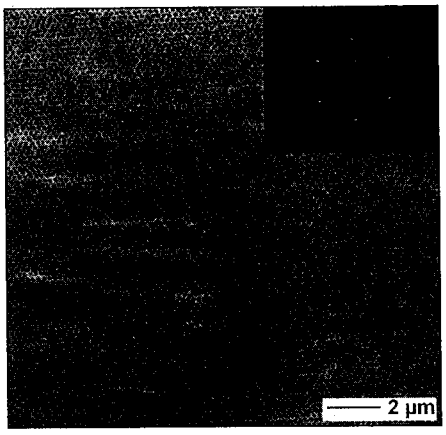

Figure 2. SEM top view of monocrystalline pore arrays in ordered porous alumina prepared with prepattern-guided anodization. The prepattern with a pitch (lattice constant) of 200 nm was induced by using electron-beam lithography. The inset shows the Fourier transform of the image.[5]

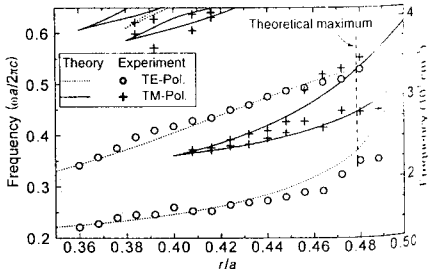

Figure 3. Bandgap edges in porous Si photonic crystals determined from transmission measurements as a function of radius/lattice constant (r/a) for a range of wavelengths. Data are shown for transverse magnetic (TM, +) and transverse electric (TE, ○) polarizations. The lattice constant was a = 1.5 μm. Calculated values for TM (solid lines) show very good agreement with the experimental data.[27]

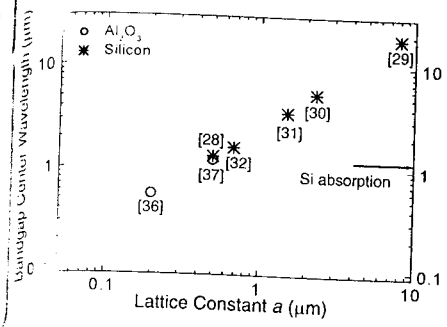

Figure 4. Summary of experimentally measured bandgap-center wavelengths for porous alumina (TE gap) and porous silicon (complete gap) as a function of the lattice constant. (From References 28–32, 36, and 37.)

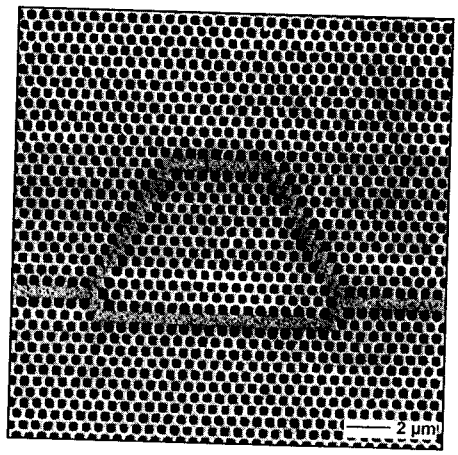

Figure 5. Top-view SEM image of a macroporous silicon photonic crystal with a lattice constant of 500 nm and an integrated two-dimensional Mach-Zehnder interferometer structure. The surface of the waveguide exhibits a small surface roughness.

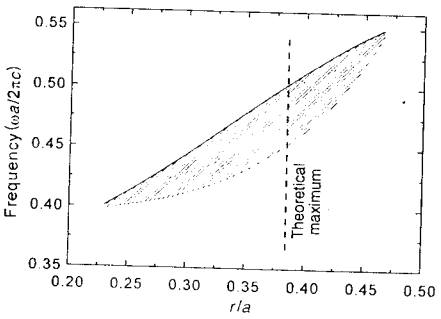

Figure 6. Bandgap map of porous alumina photonic crystals. The maximum gap for TE polarization is at r/a = 0.385 (11% gap midgap ratio). There is no gap for TM polarization in the triangular lattice. (Plane-wave expansion with 271 plane waves, ε = 2.92.)

Defects can be made in the regular porous Si structure by designing the proper lithographic mask. In this way, specific etch pits in the regular pattern are removed. Electronic holes generated at the back side by illumination are consumed by the neighboring pores without great influence on the position of these neighboring pores. The result is a relatively perfect structure with missing pores at predefined positions. These missing pores disturb the translational symmetry and lead to localized states in the forbidden spectral region. Arranging such defects in a line creates defect modes with transmission bands inside the forbidden gap. As propagation is forbidden in the surrounding medium, waveguides with very sharp bends should be possible, according to theory.[33] In the past, different defect structures have been analyzed: linear[34] and bent waveguide, Y-branch, and microresonator.[27] A 2D Mach-Zehnder interferometer with a 500-nm interpore spacing is shown in Figure 5. This device is designed to filter wavelengths based on the interference of two beams. In addition, by modulating the pore diameter, either embedded waveguides or 3D photonic crystals with a hexagonal symmetry can be obtained.[35]

Porous Alumina

The feasibility of using monodomain porous alumina as a 2D photonic-bandgap material has been predicted theoretically. Calculations show that perfectly hexagonal ordered porous alumina exhibits only a photonic bandgap for TE polarized light due to the low refractive index ($n \approx 1.7$). Figure 6 shows the calculated gap frequency range (hatched area) as a function of r/a. A maximum gap-width midgap frequency ratio of 11% is found for $r/a = 0.385$. For porous alumina, the interpore spacing that can be obtained is between 60 nm and 500 nm, leading to theoretical photonic bandgaps centered at wavelengths between 200 nm and 1300 nm, depending on the spacing. Note that the bandgap of alumina (corundum) is around 10 eV, while porous alumina has a lower bandgap due to its amorphous nature. Experimentally, however, absorption for wavelengths above 400 nm is negligible over the size of a photonic crystal. Masuda's group has recently shown transmission measurements through porous alumina photonic crystals with 200-nm and 500-nm interpore distances exhibiting photonic bandgaps around 600 nm[36] and 1300 nm[37] (see data points in Figure 4). Fabrication of more complicated integrated-optics structures seems to be difficult because lithographically defined defects (missing pores) cannot be protected during etching, as is the case for silicon.[38]

Summary

In the last 10 years, ordered pore arrays with high aspect ratios have been studied extensively. Ordered porous dielectric materials are *intrinsically* 2D photonic crystals. Although there are a large variety of materials exhibiting pores, to date only silicon and alumina exhibit the extremely high pore quality required in photonic-crystal applications. Over the last five years, the potential of macroporous silicon as an infrared photonic crystal has been described in numerous publications. Porous alumina is a favorable candidate for photonic crystals operating in the visible range.

Acknowledgments

The authors are indebted to Dr. F. Müller, Dr. A. Birner, Dr. A.P. Li, K. Nielsch, S. Matthias, Dr. K. Busch (Universität Karlsruhe) and Prof. W. Hergert (Martin-Luther-Universität, Halle) for collaboration and discussions in the area of photonic crystals. Concerning the experimental realization and characterization of the samples, the authors are grateful to Infineon Technologies and the Universities of Kiel, Konstanz, and Toronto. Special thanks go to Dr. R. Hillebrand for fruitful discussions and calculation of the bandgap map for porous alumina (Figure 6) and Prof. U. Gösele for substantially supporting the photonic-crystal activity.

References

1. For a comprehensive introduction, see J.D. Joannopoulos, R.D. Meade, and J.N. Winn, *Photonic Crystals* (Princeton University Press, New Jersey, 1995).
2. A. Uhlir, *Bell Sys. Tech. J.* **35** (1956) p. 333.
3. F. Keller, M.S. Hunter, and D.L. Robinson, *J. Electrochem. Soc.* **100** (1953) p. 411.
4. H. Masuda and K. Fukuda, *Science* **268** (1995) p. 1466.
5. A.-P. Li, F. Müller, and U. Gösele, *Electrochem. Solid-State Lett.* **3** (2000) p. 131.
6. H. Masuda, K. Yada, and A. Osaka, *Jpn. J. Appl. Phys., Part 2: Lett.* **37** (1998) p. L1340.
7. V. Lehmann and H. Föll, *J. Electrochem. Soc.* **137** (1990) p. 653.
8. V. Lehmann and U. Gösele, *Appl. Phys. Lett.* **58** (1991) p. 856.
9. J.-N. Chazalviel, R.B. Wehrspohn, and F. Ozanam, *Mater. Sci. Eng., B* **69–70** (2000) p. 1.
10. S. Langa, I.M. Tiginyanu, J. Carstensen, M. Christophersen, and H. Föll, *Electrochem. Solid-State Lett.* **3** (2000) p. 514.
11. P. Allongue, in *INSPEC Data Series*, edited by L. Canham (Institution of Electrical Engineers, London, 1997) p. 3.
12. R.L. Smith and S.D. Collins, *J. Appl. Phys.* **71** (1992) p. R1 and references therein.

13. R.B. Wehrspohn, J.-N. Chazalviel, F. Ozanam, and I. Solomon, *Phys. Rev. Lett.* **77** (1996) p. 1885.
14. R.B. Wehrspohn, J.-N. Chazalviel, F. Ozanam, and I. Solomon, *Thin Solid Films* **297** (1997) p. 5.
15. E.K. Propst and P.A. Kohl, *J. Electrochem. Soc.* **141** (1994) p. 1006.
16. M.M. Rieger and P.A. Kohl, *J. Electrochem. Soc.* **142** (1995) p. 1490.
17. R.B. Wehrspohn, J.-N. Chazalviel, and F. Ozanam, *J. Electrochem. Soc.* **145** (1998) p. 2958.
18. R.B. Wehrspohn, J.-N. Chazalviel, and F. Ozanam, *J. Electrochem. Soc.* **146** (1999) p. 3309.
19. V. Lehmann, *J. Electrochem. Soc.* **140** (1993) p. 2836.
20. V. Lehmann, *J. Electrochem. Soc.* **146** (1999) p. 2968.
21. V.P. Parkhutik and V.I. Shershulsky, *J. Phys. D: Appl. Phys.* **25** (1992) p. 1258.
22. H. Masuda, F. Hasegwa, and S. Ono, *J. Electrochem. Soc.* **144** (1997) p. L127.
23. F. Li, L. Zhang, and R.M. Metzger, *Chem. Mater.* **10** (1998) p. 2470.
24. A.P. Li, F. Müller, A. Birner, K. Nielsch, and U. Gösele, *J. Vac. Sci. Technol., A* **17** (1999) p. 1428.
25. H. Masuda, H. Asoh, M. Watanabe, K. Nishio, M. Nakao, and T. Tamamura, *Adv. Mater.* **13** (2001) p. 189.
26. A. Birner, R.B. Wehrspohn, U. Gösele, and K. Busch, *Adv. Mater.* **13** (2001) p. 377 and references therein.
27. A. Birner, A.-P. Li, F. Müller, U. Gösele, P. Kramper, V. Sandoghdar, J. Mlynek, K. Busch, and V. Lehmann, *Mater. Sci. Semicond. Proc.* **3** (2000) p. 487.
28. J. Schilling, A. Birner, F. Müller, R.B. Wehrspohn, R. Hillebrand, U. Gösele, K. Busch, S. John, S.W. Leonard, and H.M. van Driel, *Opt. Mater.* **17** (2001) p. 7.
29. U. Grüning, V. Lehmann, and C.M. Engelhardt, *Appl. Phys. Lett.* 66 (1995) p. 3254.
30. U. Grüning, V. Lehmann, S. Ottow, and K. Busch, *Appl. Phys. Lett.* **68** (1996) p. 747.
31. A. Birner, U. Grüning, S. Ottow, A. Schneider, F. Müller, V. Lehmann, H. Föll, and U. Gösele, *Phys. Status Solidi A* **165** (1998) p. 111.
32. S. Rowson, A. Chelnokov, C. Cuisin, and J.-M. Lourtioz, in *Proc. IEEE-Opto...*, Vol. 145 (Institute of Electrical and Ele... Engineers, Piscataway, NJ, 1998) p. 403.
33. S.-Y. Lin, E. Chow, V. Hietala, P.R. Villeneuve, and J.D. Joannopoulos, *Science* **282** (1998) p. 274.
34. S.W. Leonard, H.M. van Driel, A. Birner, U. Gösele, and P.R. Villeneuve, *Opt. Lett.* 25 (2000) p.1550.
35. J. Schilling, F. Müller, S. Matthias, R.B. Wehrspohn, and U. Gösele, *Appl. Phys. Lett.* 78 (2001) p. 1180.
36. H. Masuda, M. Ohya, H. Asoh, M. ...ao, M. Nohtomi, and T. Tamamura, *Jpn. J. Appl. Phys., Part 2: Lett.* **38** (1999) p. L1405.
37. H. Masuda, M. Ohya, K. Nishio, H. Asoh, M. Nakao, M. Nohtomi, A. Yokoo, and T. Tamamura, *Jpn. J. Appl. Phys., Part 2: Lett.* 39 (2000) p. L1039.
38. H. Masuda, M. Yotsuya, M. Asana, K. Nishio, M. Nakao, A. Yokoo, and T. Tamamura, *Appl. Phys. Lett.* **78** (2001) p. 826.